Comparison of the Electrochemical Lithiation/Delitiation Mechanisms of FeP_x ($x = 1, 2, 4$) Based Electrodes in Li-Ion Batteries

S. Boyanov,[†] D. Zitoun,[†] M. Ménétrier,[‡] J. C. Jumas,[†] M. Womes,*[,†] and L. Monconduit*[,†]

Institut Charles Gerhardt Montpellier-UMR 5253 CNRS-UM2-ENSCM-UM1 Agrégats, Interfaces et Matériaux pour l'Energie CC 1502, Place Eugène Bataillon, 34095 Montpellier, France, and Université de Bordeaux, ICMCB, 87 Avenue Schweitzer, F-33608 Pessac Cedex, France

Received: June 29, 2009; Revised Manuscript Received: October 22, 2009

The electrochemical reaction mechanisms of FeP_x ($x = 1, 2, 4$) as electrode materials in Li batteries were analyzed by ^{57}Fe Mössbauer spectroscopy, magnetic and NMR measurements. Depending on their stoichiometry, iron phosphides react with lithium along different pathways. FeP and FeP_2 are fully or partially converted to a composite electrode of Li_3P and Fe. For both, the same intermediate phases, namely FeP and Li_xFeP, were identified in cycling and FeP is partially regenerated on charge. Surprisingly, FeP_4 reacts with Li through an insertion type process previously identified for earlier transition metal phosphides (Ti, V, and Mn), and no conversion reaction to Li_3P/Fe is observed. The long-term stability of the composite electrode Li_3P/Fe^0 and of the intermediate phase Li_xFeP is analyzed.

1. Introduction

New developments in the field of renewable energies, electric vehicles, and portable electronics have led to an increasing demand for advanced energy storage devices in recent years. The characteristics of these storage devices like mass and volume capacity or maximum charge and discharge rates have to be adapted to the requirements of the respective application. As a consequence, many efforts have been undertaken to improve the performances of carbon-based materials,[1–3] which constituted the first commercialized negative electrode in "lithium-ion" batteries (by Sony Energytech).[4] As an alternative approach, attempts were made to substitute the carbon electrode by materials with more favorable properties. In this context, the promising behavior of transition metal phosphides was underlined in several studies.[5–9]

Our own recent work on iron phosphide, FeP, revealed a complex lithiation/delithiation mechanism characterized by a direct conversion of the starting material in the first discharge to Li_3P and Fe metal.[10,11]

$$FeP + 3Li \rightarrow Li_3P + Fe \quad (1)$$

The following recharge and all successive discharge/charge cycles can be described as a combination of a conversion

$$Li_3P + Fe \leftrightarrow Li_xFeP \quad (2)$$

and an insertion/deinsertion reaction

$$Li_xFeP \leftrightarrow FeP + x\,Li \quad (3)$$

The insertion/deinsertion reaction (3) is highly reversible, leading to a capacity retention of 300 mAh g^{-1} and 1900 mAh cm^{-3} after 100 cycles and corresponds to the formation/destructuration of an intermediate tetragonal ternary phase.

Considering the good electrochemical performances found for FeP, linked to the formation of Li_3P upon discharge, even higher capacities can be expected from the reaction of FeP_x with lithium when x is increased from 1 to 4. A comparison of the electrochemical behavior of the iron phosphides FeP_x ($x = 1$, 2, 4) is also interesting from a fundamental point of view as their crystallographic structures are characterized by more or less open atomic arrangements, a factor which strongly influences the reaction mechanism with lithium.

Concerning the experimental techniques to be used for the phase analysis in lithiated or delithiated iron phosphide electrodes, our previous study on FeP had shown that the only phase that can be detected by XRD throughout the processes (1) to (3) was Li_3P. All other phases were formed as nanosized XRD-amorphous particles. We therefore combined in ref 11 ^{57}Fe Mössbauer spectroscopy with measurements of magnetic moments and magnetic susceptibilities for a more detailed phase analysis. This coupled approach was a powerful tool to analyze FeP electrode materials due to the different magnetic properties of the involved phases (antiferromagnetic FeP, ferromagnetic Fe, and paramagnetic LiFeP). The two techniques are complementary insofar as measurements of the magnetic susceptibilities allow detecting even small amounts of a ferromagnetic phase (like metallic iron), provided all other phases present are dia- or paramagnetic or give only a weak signal like antiferromagnetic compounds. Their detection is possible even in cases where Mössbauer spectroscopy fails to reveal them unambiguously due to overlap with absorption lines of other phases. On the other hand, the presence of paramagnetic compounds (like LiFeP), even when X-ray amorphous, is easily demonstrated by Mössbauer spectroscopy.[11]

In the present study we used the same approach as in ref 11 and completed our data set by results from ^7Li and ^{31}P NMR to explore the electrochemical mechanisms of FeP_2 and FeP_4 and to compare them with the mechanism revealed from the study of FeP. We further address in the present paper the question of the stability of intermediate reaction products formed during

* To whom correspondence should be addressed.
[†] Institut Charles Gerhardt Montpellier.
[‡] Université de Bordeaux.

10.1021/jp906080j CCC: $40.75
Published on Web 11/24/2009

electrochemical cycling. This question is of importance for the analytical approach used to identify electrochemical reaction products as well as for the practical use of these materials in batteries. It will be shown that the delay between the end of the electrochemical reaction and the sample analysis has to be kept as short as possible.

2. Experimental Section

Sample Preparation. The orthorhombic FeP (*Pnma*) and FeP_2 (Pmnn) phases and the monoclinic FeP_4 ($P2_1/c$) phase were synthesized from stoichiometric mixtures of powders of the elements (Fe: Alfa Aesar, 350 mesh, 99.9%; P: Alfa Aesar, 100 mesh, 99%) following protocols described elsewhere.[12] The mixtures for the binaries were heated in evacuated silica ampules to a temperature of 973 K for 5 days and then cooled to room temperature by quenching. Li_3P was synthesized by ball milling during 18 h using a Retsch 200 mixer mill that generates normal mechanical strain. The grinding vial loading was done in an argon-filled glovebox. Required amounts of Li and red P precursor powders were placed in a stainless steel container together with steel balls in a weight ratio of steel ball to powder of 24:1.[13]

Electrochemical Tests. Electrochemical discharge and charge runs were carried out in Swagelok test cells connected to a VMP or a MacPile automatic cycling and data recording system (Biologic Co., Claix, France). The cells were assembled in a glovebox under argon and comprised a lithium metal disk as the negative electrode, a Whatman GF/D borosilicate glass fiber sheet saturated with a solution of 1 M $LiPF_6$ in ethylene carbonate/dimethyl carbonate (1:1 by weight) as the electrolyte, and a mixture of the iron phosphide with 15 weight percent carbon black (SP) as the positive electrode. Usually, 10−12 mg of mixed (85/15 wt %) iron phosphide and carbon black were used in the tests which were carried out at C/10 scan rates (1 Li in 10 h per formula unit) in a potential window between 2.5 and 0.0 V versus Li^+/Li^0.

Sample Characterization. X-ray diffraction (XRD) on pristine FeP, FeP_2, and FeP_4 was performed on a Philips X'Pert diffractometer using Cu Kα radiation. In situ X-ray diffraction was carried out using electrochemical cells similar to the Swagelok cells but equipped with a beryllium window as the current collector on the X-ray side. The cells were connected to a VMP system and discharged and charged at a C/20 rate while being placed on a Philips X-pert diffractometer (Cu Kα radiation). Diffraction patterns were recorded dynamically for every 0.1 Li reacted, using potential steps of 5 mV.

Magnetic Properties. Magnetizations were measured on a Superconducting Quantum Interference Design (SQUID) magnetometer MPMS XL7 between 2 and 300 K in magnetic fields between 0 and 5 T. The temperature dependent susceptibility was measured using a DC procedure. The sample was first cooled to 2.0 K under zero magnetic field, and then data were recorded in a low magnetic field of 5−50 mT between 2 and 300 K (zero-field cooled, ZFC). Field-cooled (FC) measurements were performed from 2 to 300 K after cooling the sample in an applied field. Measurements on electrode materials were carried out ex situ, after extraction of the electrode material from the Swagelok cell. The results are given with respect to the effective mass of iron contained in the sample, after correction for added carbon black and inserted lithium.

Mössbauer Spectroscopy. Mössbauer spectra were recorded in the constant acceleration mode and in transmission geometry on a standard Mössbauer spectrometer composed of components from Ortec and Wissel. A $^{57}Co(Rh)$ source with a nominal activity of 10 mCi was used. Low temperature spectra were recorded by cooling the sample in a flow cryostat from l'Air Liquide, using liquid nitrogen or liquid helium as cooling agent. The source was always kept at room temperature. The hyperfine parameters isomer shift (δ), hyperfine magnetic field (H), quadrupole splitting (ΔE_q, for $H = 0$), and quadrupolar perturbation ($2\epsilon'$, for $H \neq 0$) of the various species were determined by fitting Lorentzian lines to the experimental data, using the ISOfit program.[14]

Isomer shifts are given with respect to the center of the six-line spectrum of an α-Fe foil recorded at room temperature. Mössbauer spectra of electrode materials were recorded ex situ after transferring the material under argon atmosphere from the Swagelok cell to a specific airtight sample holder equipped with gamma-transparent windows. Each spectrum along the discharge/recharge cycle was recorded on a separate, individual sample.

NMR Spectroscopy. ^{31}P and ^{7}Li MAS NMR measurements were carried out with a Bruker Avance 300 spectrometer, using a standard Bruker 2.5 mm MAS probe, at a 30 kHz spinning speed. Materials recovered from positive electrodes were placed in the rotors in an Ar-filled glovebox. For ^{31}P (121 MHz), a Hahn echo pulse sequence (with refocusing delay equal to one rotor period i.e. 33.3 μs) was used. The 90° pulse was 1.7 μs, and the recycle delay was 60 s. The reference is H_3PO_4 (85%). For ^{7}Li experiments (116 MHz), a single pulse was used with a 2.2 μs 90° pulse and a 20 s recycle delay. The 0 ppm reference is LiCl 1 M in aqueous solution.

3. Results

3.1. Crystal Structures and Sample Morphologies. X-ray powder diffractograms showed that FeP and FeP_2 were obtained in pure form while FeP_4 contained impurities of FeP and FeP_2 (Figure 1). According to scanning electron microscopy (SEM), the as-obtained FeP and FeP_4 powders are made of particles without well-defined shapes having an average size ranging from 5 to 50 μm, whereas the FeP_2 powder consists of crystallized particles with same size and well-defined shape.

The FeP structure can be viewed as a closely packed FeP_6 face-sharing structure with Fe−P covalent bonds presenting a high degree of covalence.[15,16] Within the FeP unit cell, Fe is coordinated by 6 P atoms in a nearly hexagonal configuration with Fe−P distances between 2.186 and 2.447 Å.

Compared to FeP, the crystal structure of FeP_2 is less compact. Iron atoms in FeP_2 are also located in FeP_6 octahedra forming parallel edge-sharing chains interconnected by corners (one type of Fe and one type of P per unit cell).[17] The structure of FeP_4 consists of corrugated monolayers of Fe atoms (perpendicular to the (100) direction) separated by double layers of P atoms, leading to two types of Fe and six types of P in the unit cell. The Fe atoms sit in FeP_6 octahedra sharing some of their edges and/or corners, and the P atoms form a 3D network of P−P bonds within each double layer.[18]

3.2. Electrochemistry. Before detailing the electrochemical results that were obtained for FeP_x with $x = 1$, 2, and 4, it is important to point out that the FeP_x phases with $x = 0.33$ and 0.5 showed no reaction versus lithium.[19]

Panels a, c, and e and b, d, and f in Figure 2 show the first three sweeps of the voltage versus lithium curve of FeP, FeP_2, and FeP_4 and the derivative $-dx/dV$ vs potential, respectively, acquired at a C/10 rate between 2.5 and 0 V.

For FeP a potential plateau at 0.1 V is observed during the first discharge. As previously stated this plateau characterizes a two-phase reaction associated with the insertion of 2.8 Li, corresponding to an initial capacity of 880 mAh/g.[10] Upon

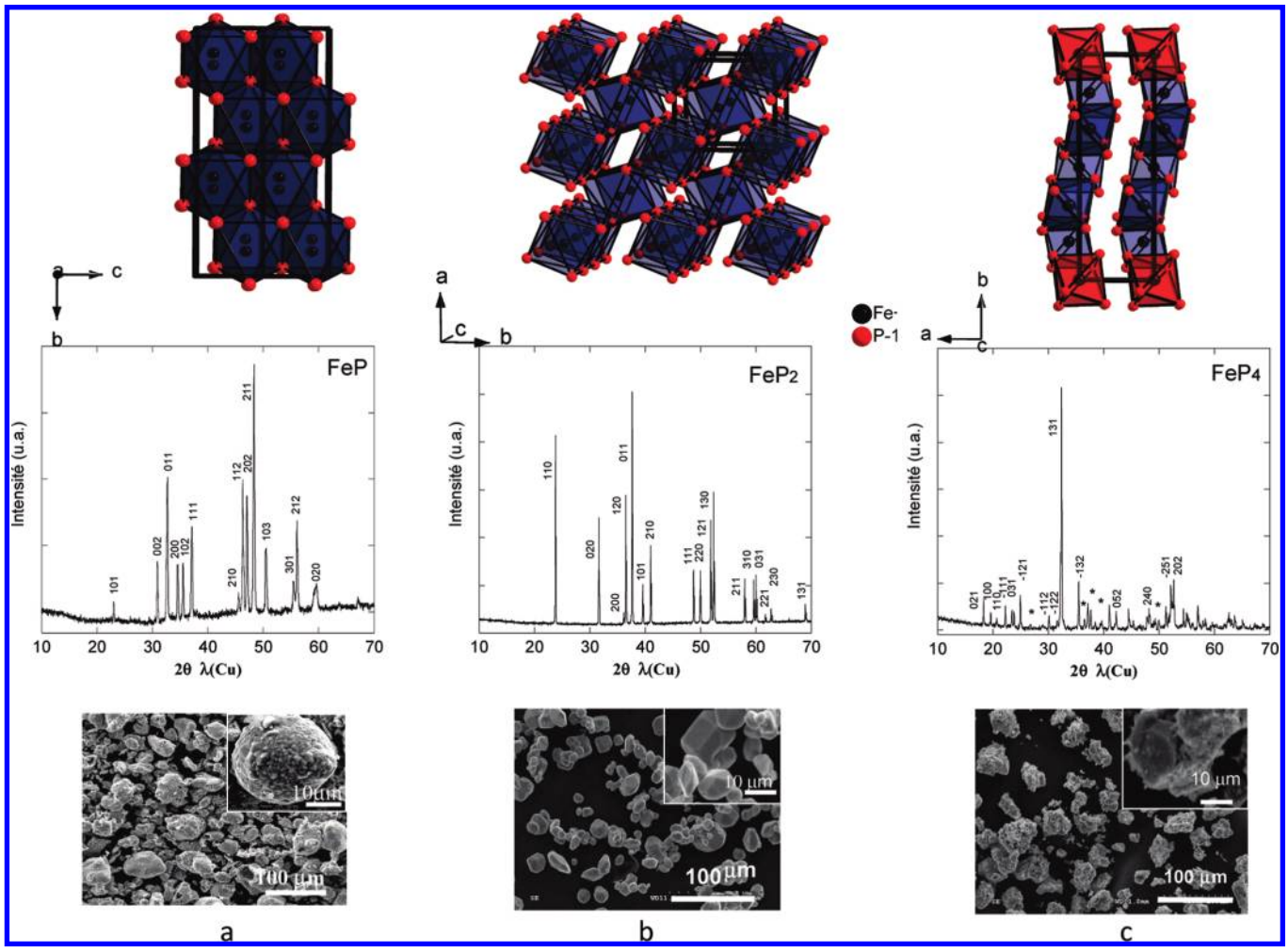

Figure 1. Powder X-ray diffraction pattern, SEM images and crystallographic cells of FeP (a), FeP2 (b), and FeP4 (c). Stars indicate the FeP and FeP2 impurity traces in the FeP4 pattern.

charge, 2.4 Li are extracted from the electrodes, leading to a reversible capacity of 720 mAh/g (4450 mAh/cm^3) and to a 18% capacity loss during the first cycle. The derivative curve reveals the presence of two distinct processes A and B during oxidation, occurring at 0.9 V (A) and 1.1 V (B). The second discharge of the battery differs from the first one. Two processes are distinguished at 0.55 V (B′) and at 0.2 V (A′) instead of the low potential reaction with lithium at 0.1 V observed during the first discharge.

For FeP_2, (Figure 2c,d) a potential plateau at 0.3 V is observed during the first discharge. This plateau characterizes a two-phase reaction involving 4.4 Li, corresponding to an initial capacity of 1000 mAh/g. Upon charge, 2.9 Li are extracted from the electrodes, leading to a reversible capacity of 653 mAh/g (3300 mAh/cm^3) and to a 34% capacity loss during the first cycle. The derivative curve reveals the presence of two distinct processes A and B during oxidation, occurring at 0.9 V (A) and 1.1 V (B). The second discharge of the battery differs from the first one. Two processes are distinguished at 0.65 V (B′) and 0.55 V (A′) instead of the low potential reaction with lithium at 0.3 V observed during the first discharge.

The cycleability in the 0−2 V potential window is not improved by changing the cycling rate to C/5 or C/20. On the other hand a 300 mAhg^{-1}capacity is maintained on the limited 0.55−2 V potential window (see S1; after an initial discharge down to 0 V).

For FeP_4 (Figure 2e,f) a potential plateau at 0.5 V is observed during the first discharge corresponding to the insertion of 5.25 Li. Two small plateaus following at 0.25 and 0.1 V can be attributed to impurities of FeP_2 and FeP, respectively, so that in total 6.6 Li are inserted in the electrode. Upon charge, a single plateau is observed at 1.1 V (peak labeled A in Figure 2f). 3.6 Li are extracted from the material, corresponding to a reversible capacity of 530 mAh/g (2184 mAh/cm^3) and to a capacity loss of 47% during the first cycle. The second discharge curve is clearly different from the first. A plateau at 0.75 V is now observed (peak labeled A′ in Figure 2f) instead of the main plateau at 0.5 V of the first discharge. Furthermore, the plateaus at 0.25 and 0.1 V of the impurities have disappeared.

3.3. X-ray Diffraction. ***FeP.*** An in situ X-ray diffraction (XRD) analysis of the discharge of an FeP electrode was already presented in ref 10. It demonstrated unambiguously the destruction of the pristine FeP and the formation of Li_3P at the end of the first discharge. In some cases a small amount of residual FeP was observed at the end of this process indicating an incomplete reaction.

FeP_2. Figure 3A-a shows the diffraction pattern of the starting FeP_2 material, whereas the pattern of mechanochemically synthesized Li_3P is shown in Figure 3A-b. The XRD analysis of a FeP_2 electrode performed at the end of the first discharge (Figure 3A-c) reveals large Bragg peaks at 24°, 26°, and 42° 2θ attributed to the formation of Li_3P with low crystallinity and smaller particle size than the mechanochemically obtained Li_3P. Some diffraction peaks of FeP_2 were still observed, indicating the incomplete conversion of the starting material. Iron metallic

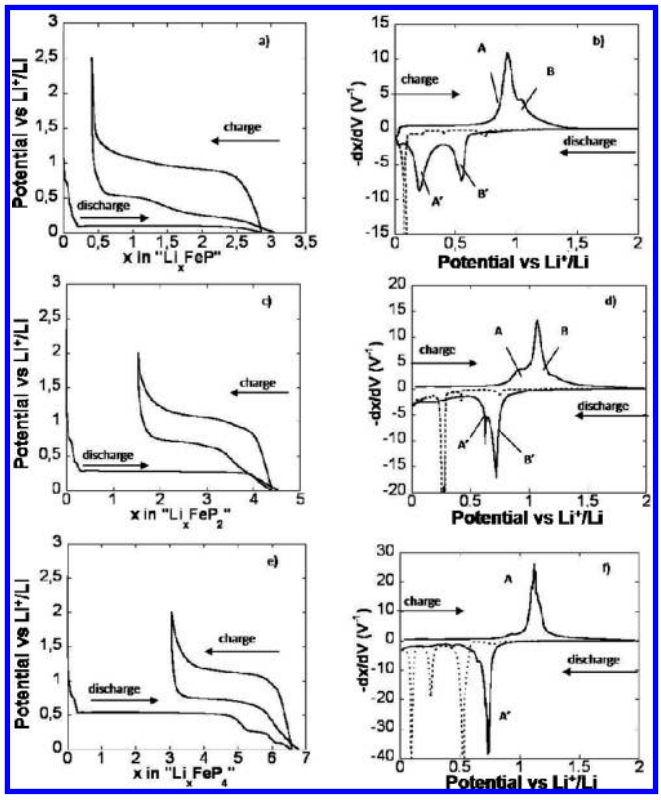

Figure 2. First cycles of FeP, FeP_2, and FeP_4 electrodes versus lithium, plotted as the electrochemical potential vs the number x of lithium atoms inserted (a, c, and e for FeP, FeP_2, and FeP_4, respectively) and as the derivative $-dx/dV$ vs potential (b, d, and f for FeP, FeP_2, and FeP_4, respectively). Dashed line: first discharge; solid line: first charge and second discharge.

phase is probably not present in X-ray pattern because of the very small cluster size.

FeP_4. Figure 3B shows in situ X-ray diffraction patterns recorded during the first discharge run of FeP_4 until insertion of a total number of 5 Li atoms per formula unit. This point corresponds to the end of the 0.5 V plateau seen in Figure 2e. At this point, a formal stoichiometry of Li_5FeP_4 is thus reached. The diffraction patterns show the progressive reduction in intensity of the peaks of FeP_4 and the appearance of rather broad peaks of a new phase at 25.9, 30.1, and 42.5° 2θ, marked with arrows. Comparison of the peak positions of this new phase with a X-ray diffraction database reveals close similarities with the ternary phase Li_7MnP_4.[20] We thus tentatively attribute these new diffraction peaks to a ternary phase Li_5FeP_4 so far not described in the literature. Ternary Li_xMPn_4 phases (M = Ti, V, Mn) are known to crystallize either in the centro-symmetric $Fm\bar{3}m$ (no. 225) space group or in the non centro-symmetric $F\bar{4}3m$ (no. 216) space group.[21–23] In both structures, pnictogen atoms Pn lie on the 4-fold 4a (0,0,0) crystallographic positions with the $m\bar{3}m$ and $\bar{4}3m$ symmetries, respectively. They form an fcc unit cell in which 12 (4 octahedral and 8 tetrahedral) Pn-coordinated cationic vacancies are available. Depending on both the lithium content and the cationic distribution, such as ordering of M and Li on tetrahedral sites, cells adopt either the $Fm\bar{3}m$ symmetry or the $F\bar{4}3m$ symmetry.

Although XRD gave some first indications on the reaction mechanism, the analysis has to be completed by other techniques in order to check for the eventual presence of X-ray amorphous phases. For example, no indication on the presence of metallic iron expected for discharged FeP_2 was found in the diffractograms. Thus, like in our previous work on FeP, further investigations by measurements of the magnetic susceptibilities, ^{57}Fe Mössbauer spectroscopy, and NMR spectroscopy were carried out.

3.4. ^{57}Fe Mössbauer Spectroscopy. *FeP.* FeP was already analyzed in detail in a previous work (ref 11). ^{57}Fe Mössbauer spectra revealed the formation of metallic iron according to reactions 1 and 2. A further phase appearing in the spectra was interpreted as ternary Li_xFeP according to reaction 3. Its Mössbauer parameters isomer shift ($\delta = 0.27 \pm 0.02$ mm/s) and quadrupolar splitting ($\Delta E_q = 0.29 \pm 0.03$ mm/s) are close to those of synthesized LiFeP ($\delta = 0.24 \pm 0.07$ mm/s; $\Delta E_q = 0$[11]), the nonzero quadrupolar splitting of the electrochemically formed phase being explained by a stoichiometry deviating from the $Li_{1.0}FeP$ composition. This ternary phase was observed in important amounts beginning with the first recharge. The Li_xFeP/FeP ratio increased and decreased during subsequent cycling in agreement with reactions 2 and 3. However, none of these reactions was entirely completed. Considerable amounts of FeP and Li_xFeP were observed at any moment of further cycling. Only the consumption of metallic Fe in reaction 2 was completed.

FeP_2. Figure 4 shows a series of ^{57}Fe Mössbauer spectra of FeP_2 recorded at different stages of discharge and charge runs. The hyperfine parameters isomer shift (δ), quadrupolar splitting (ΔE_q), quadrupolar perturbation ($2\epsilon'$), and hyperfine magnetic field (H) of all samples are given in Table 1. Figure 4a shows the ^{57}Fe Mössbauer room temperature spectrum of the starting material, the hyperfine parameters of which agree well with literature.[24] The spectrum of Figure 4b was recorded at room temperature at the end of the first discharge. We observe the doublet of FeP_2, indicating incomplete conversion of the starting material, and two additional doublets with hyperfine parameters very close to those of FeP and the ternary phase Li_xFeP already observed in FeP electrodes. Furthermore, a singlet at zero velocity is seen, indicating the presence of very small iron particles. Each particle forms a single magnetic domain as soon as its size falls below the Bloch wall scale (few tens of nanometers). The magnetization vector of such particles switches rapidly from one direction of easy magnetization to another (superparamagnetism). When the time it spends in one direction becomes shorter than the characteristic measuring time of Mössbauer spectroscopy τ_M, then the time-averaged magnetic field seen by the nucleus becomes zero and the particles appear as nonmagnetic. In the present case τ_M is given by the period of the Larmor precession of the ^{57}Fe nuclear magnetic moment ($\tau_M \cong 5 \times 10^{-9}$ s in the field of 33 T of bulk α-Fe[25]). The spectrum of the same sample recorded at 77 K (Figure 4c) can be fitted with one singlet, one sextet, and two doublets. The doublet with the larger quadrupole splitting stems from residual FeP_2 while the second doublet represents FeP together with the ternary phase Li_xFeP which are difficult to distinguish in this spectrum due to the lower resolution on this larger velocity scale necessary for the detection of magnetically ordered iron. The sextet confirms the presence of a magnetically ordered phase. At this lower temperature the fluctuation of the magnetization is sufficiently slowed down for some of the particles that they appear now as magnetically blocked. We attribute the strong broadening of the absorption lines and the rather low magnetic field of approximately 21 T as compared to bulk α-Fe (33.9 T at 77 K) to the small size of the metallic particles, resulting in a high fraction of surface atoms with a reduced number of magnetic neighbors.[26,27] The magnetization of surface atoms decreases more rapidly with temperature than that of core atoms.[28] The line width of 1.5 mm/s shows that the distribution

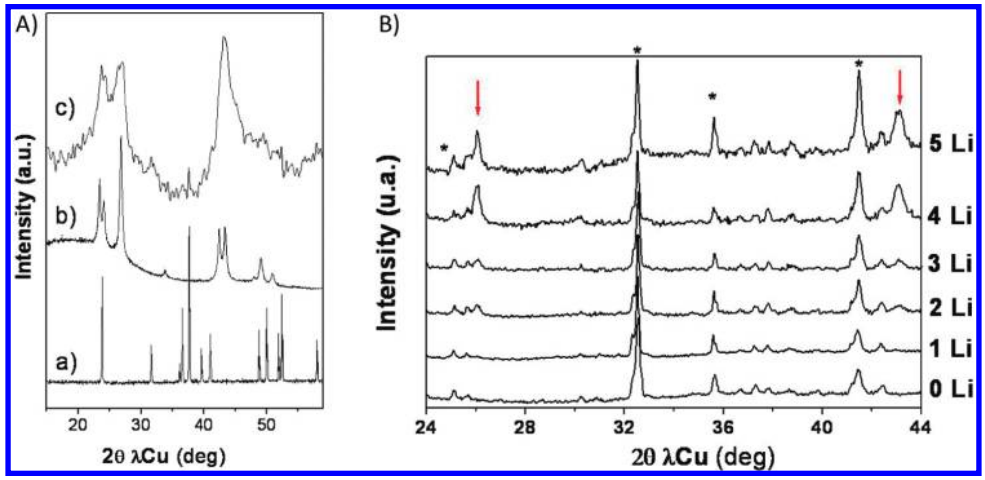

Figure 3. (A) X-ray powder diffractograms of (a) FeP_2 starting material, (b) Li_3P obtained by mechano-synthesis, (c) a FeP_2 electrode at the end of the first discharge. (B) X-ray diffractograms recorded in situ on FeP_4 electrodes during the first discharge. The red arrows indicate main Bragg peaks of the ternary phase.

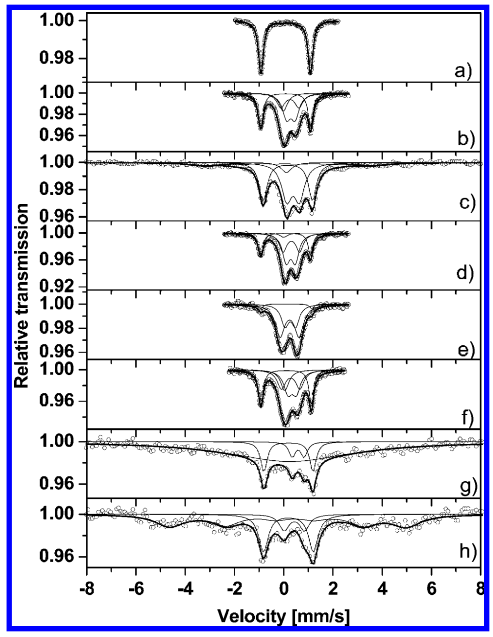

Figure 4. Mössbauer spectra of FeP_2 electrodes at various depths of lithiation; spectrum of the starting material recorded at 295 K (a), end of first discharge at 295 K (b) and 77 K (c), half recharge at 295 K (d), complete recharge at 295 K (e), complete second discharge at 295 K (f), 75 K (g), and 20 K (h).

of magnetic fields extends from 16 to 26 T. A singlet at 0.1 mm/s indicates the presence of very small iron particles exhibiting still an averaged nonmagnetic behavior. The total spectral weight of metallic iron derived from spectrum 4c amounts to 22%.

In the middle (1 V) and at the end of the first charge (2 V), the room temperature spectra (Figure 4d,e) can be fitted with three doublets, ascribable to residual FeP_2, FeP, and Li_xFeP. At 1 V some superparamagnetic iron is still observed in addition, which has disappeared at 2 V. The Li_xFeP/FeP ratio is higher at 1 V than at 2 V. It is worth noting that the relative amount of FeP_2 detected by Mössbauer spectroscopy decreases during the charge process.

The room temperature spectrum recorded at the end of the second discharge (Figure 4f) shows the characteristic singlet at zero velocity of superparamagnetic iron particles with time-averaged zero magnetic field and the doublets of FeP, Li_xFeP, and FeP_2. A spectrum of the same sample recorded at 75 K (Figure 4g) reveals the presence of a magnetically ordered phase. The particle size of this phase is, however, smaller than that of the magnetic phase found after the first discharge (Figure 4c). As a consequence, the fluctuation rate of the magnetization of these particles is higher than for sample 4c and the six-line spectrum collapses toward a broadened singlet. Further lowering of the temperature to 20 K (Figure 4h) slows down the fluctuation sufficiently to give rise to the characteristic six-line splitting. The magnetic field of approximately 30 T and the isomer shift of approximately 0.3 mm/s are close to the characteristic values of bulk α-Fe. We note that the amount of FeP_2 is higher than at the end of the previous charge.

FeP_4. Figure 5a shows the room temperature spectrum of the FeP_4 starting material. The spectrum of FeP_4 consists of two doublets with a 2:1 intensity ratio, in agreement with the crystal structure of FeP_4 where iron atoms occupy two crystallographically different sites.[18] The hyperfine parameters δ and ΔE_q of the two doublets, given in Table 2, are quite close to those reported in the literature.[28] The spectrum reveals the presence of a minor amount of FeP_2 responsible for the plateau at 0.3 V observed in the discharge curve (Figure 2e). A small impurity of FeP also revealed by the discharge curve could be masked in the spectrum by the two doublets of FeP_4. The low temperature Mössbauer spectrum recorded at 77 K (not shown) provides no further information on the material.

At the end of the first discharge, the spectral shape suggests the presence of residual FeP_4 and FeP_2 (Figure 5b). A substantial change in shape indicates, however, the appearance of one or several new phases. A fit of the spectrum supposing the presence of FeP and a ternary phase Li_xFeP with hyperfine parameters similar to those found for FeP and FeP_2 electrodes gives a satisfying agreement with the experimental data. The low temperature spectrum recorded at 77 K (Figure 5c) gives no indication on the presence of magnetically ordered metallic iron.

At the end of the first charge (Figure 5d), the ternary phase has disappeared. However, a noticeable amount of FeP is conserved which might stem from a partial electrochemical conversion of FeP_2 in addition to the small amount already present in the pristine material. The room temperature spectrum obtained at the end of the second discharge (Figure 5e) resembles closely that of the first discharge and obviously the same ternary phase is formed.

3.5. Magnetic Properties. Measurements of the saturation magnetization at 2 K were carried out for the quantitative

TABLE 1: Hyperfine Parameters of the Phases Observed during Discharge and Charge of FeP_2[a]

spectrum on Figure 4	number of lithium atoms	temperature [K]	δ [mm/s]	ΔE_q or $2\epsilon'$ [mm/s]	2Γ [mm/s]	H [T]	spectral weight [%]	identification
a	0.0	295	0.08(1)	2.01(1)	0.24(1)	0.0	100	FeP_2
b	4.4	295	0.08(1)	2.02(1)	0.25(1)	0.0	31	FeP_2
			−0.02(3)	0.00	0.40(2)[b]	0.0	14	Fe (sp)
			0.25(2)	0.73(3)	0.40(1)(1)[b]	0.0	21	FeP
			0.29(2)	0.34(2)	0.40(5)(1)[b]	0.0	34	Li_xFeP
c	4.4	77	0.17(1)	2.00(1)	0.39(1)	0.0	36	FeP_2
			0.11[c]	0.00	0.50[c]	0.0	6	Fe (sp)
			0.20[c]	0.00	1.5(3)	21.4(8)	16	Fe (b)
			0.38(1)	0.51(1)	0.50[c]	0.0	41	FeP + Li_xFeP
d	3.5	295	0.08(1)	2.02(2)	0.24(1)	0.0	23	FeP_2
			0.00[c]	0.00	0.37(1)[b]	0.0	4	Fe (sp)
			0.31(1)	0.67(2)	0.37(2)[b]	0.0	30	FeP
			0.28(1)	0.37(1)	0.37(2)[b]	0.0	43	Li_xFeP
e	1.5	295	0.10(2)	2.06(2)	0.22(5)	0.0	4	FeP_2
			0.24(1)	0.77(2)	0.45(2)	0.0	62	FeP
			0.26(1)	0.43(4)	0.38(4)	0.0	34	Li_xFeP
f	4.5	295	0.08(2)	2.02(1)	0.24(1)	0.0	29	FeP_2
			0.03(4)	0.00	0.40(1)[b]	0.0	15	Fe (sp)
			0.26(2)	0.74(4)	0.40(9)[b]	0.0	26	FeP
			0.32(2)	0.33(3)	0.40(2)[b]	0.0	30	Li_xFeP
g	4.5	75	0.19(1)	2.00(2)	0.32(3)[b]	0.0	13	FeP_2
			0.11[c]	0.00	6.2(6)	0.0	81	Fe (sp)
			0.59(3)	0.50(3)	0.32(3)[b]	0.0	6	FeP + Li_xFeP
h	4.5	20	0.20(2)	2.04(3)	0.46(6)[b]	0.0	28	FeP_2
			0.12[c]	0..0	1.6(2)	29.8	60	Fe (b)
			0.44(4)	0.87(6)	0.46(4)[b]	0.0	12	FeP + Li_xFeP

[a] The quadrupole splitting ΔE_q is given for paramagnetic samples ($H = 0$) and the quadrupolar perturbation $2\epsilon'$ for magnetically split spectra ($H \neq 0$). The magnetic properties are indicated as blocked (b) or superparamagnetic (sp). [b] Parameters constrained to be equal. [c] Parameter kept fixed in the refinement.

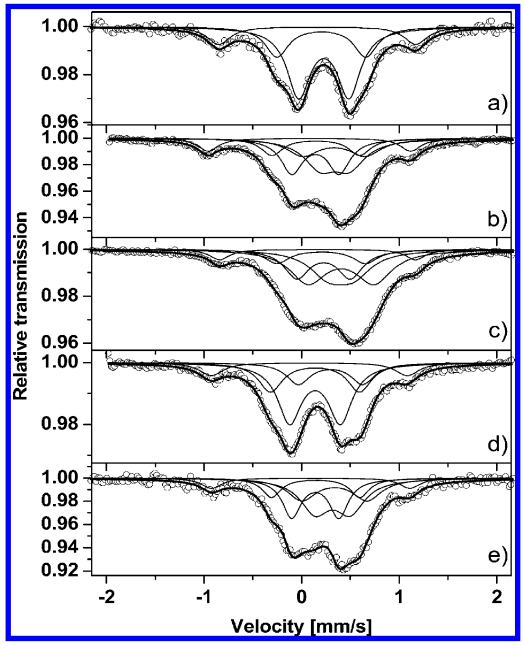

Figure 5. Mössbauer spectra of FeP_4 electrodes at various depths of lithiation; spectrum of the starting material recorded at 295 K (a), end of first discharge at 295 K (b) and 77 K (c), end of first recharge at 295 K (d), end of second discharge at 295 K (e).

detection of metallic iron. The size of the iron particles was deduced from the blocking temperature of the magnetization determined by fitting the zero-field cooled and field cooled (ZFC/FC) magnetic susceptibilities with an assembly of isolated magnetic nanoparticles, assuming a log-normal size distribution.

FeP. Magnetization measurements were previously performed for the FeP sample at different discharge depths and the main results indicated a typical ferromagnetic behavior. The results are resumed in Table 3.[11]

The reaction of FeP with lithium during the first discharge led to a progressive increase of the saturation magnetization, which allowed us to conclude on the effective formation of iron particles. At the end of the discharge, 75% of the pristine material is transformed to metallic iron, assuming that the electrochemically formed iron carries a magnetic moment close to the bulk value.

Upon charge, while a strong decrease of the saturation magnetization was measured during reaction 2 (process A in Figure 2b) between 0 and 1 V, no further decrease of the magnetization was observed during reaction 3 between 1 and 2 V (process B). The second discharge was characterized by a new increase of the magnetization. At 1.5 Li (0.4 V, end of reaction 3 and of process B′), the magnetization has slightly increased indicating the beginning formation of iron particles, while at the end of the second discharge a value of 65 Am^2/kg_{Fe} is reached corresponding to an amount of metallic iron of about 30%.

At room temperature, the sample exhibited superparamagnetic behavior, as deduced from the zero coercivity field and the zero remanent magnetization, resulting from the small particle size and the high degree of dispersion of iron nanoparticles in the Li_3P matrix, leading to isolated, magnetically not interacting particles. At 2 K, the magnetization vectors are blocked and a ferromagnetic behavior was observed, characterized by a coercivity field of 0.028 T and a remanent magnetization $M_r = 2.7$ Am^2/kg_{Fe} ($M_r/M_s = 0.11$).

ZFC/FC measurements of the magnetic susceptibilities were carried out with the aim to gain more information about the radii of the iron particles. At the end of the first and second discharge, the ZFC-FC curves show a ferromagnetic behavior with a blocking temperature above 300 K, indicating properties

TABLE 2: Hyperfine Parameters of the Phases Observed during Discharge and Charge of FeP_4

spectrum in Figure *5*	number of lithium atoms	temperature [K]	δ [mm/s]	ΔE_q [mm/s]	2Γ [mm/s]	spectral weight [%]	identification
a	0.0	295	0.15(1)	0.49(1)	0.27(1)[a]	58	FeP_4
			0.15(1)	0.90(1)	0.27(2)[a]	29	FeP_4
			0.08(1)	2.02(2)	0.22(2) 29	13	FeP_2
b	6.6	295	0.14[b]	0.48(1)	0.27(1)[a]	26	FeP_4
			0.15[b]	0.90(1)	0.27(1)[a]	13	FeP_4
			0.08(1)	2.08(2)	0.26(2)	10	FeP_2
			0.33(2)	0.64(3)	0.40(2)[a]	20	FeP
			0.34(1)	0.30(2)	0.40(1)[a]	31	ternary phase
c	6.6	77	0.23[b]	0.55[b]	0.31(1)[a]	22	FeP_4
			0.20[b]	0.91[b]	0.31(1)[a]	11	FeP_4
			0.16(1)	2.01(2)	0.25(2)	6	FeP_2
			0.40(1)	0.68(2)	0.45(2)[a]	35	FeP
			0.40(1)	0.26(2)	0.45(1)[a]	26	ternary phase
d	3.0	295	0.14(1)	0.52(1)	0.30(1)[a]	48	FeP_4
			0.14(3)	0.91(3)	0.30(2)[a]	24	FeP_4
			0.08(1)	2.01(2)	0.30(3)	11	FeP_2
			0.30(3)	0.66(3)	0.30(1)	17	FeP
e	6.8	295	0.15[b]	0.48[b]	0.23(1)[b]	26	FeP_4
			0.15[b]	0.90[b]	0.23(1)[b]	13	FeP_4
			0.09(2)	2.03(3)	0.26[b]	8	FeP_2
			0.34(3)	0.67(4)	0.36(3)[a]	22	FeP
			0.32(2)	0.36(3)	0.36(1)[a]	33	ternary phase

[a] Parameters constrained to be equal. [b] Parameter kept fixed in the refinement.

TABLE 3: Magnetic Moment Deduced from the High Field Measurements[a]

starting material	Li uptake voltage/Li	M_{sat} ($A.m^2/kg_{Fe}$)	%Fe	$T_{blockage}$ (K)	$R_{mean} \pm s$ (nm)	K_v (J/m^3)
FeP	0 Li	6.2				
	2.8 Li; 0 V	150	75.2	>300	>7.1	$7\ 10^4$
	3.0 Li; 0 V	65.0	32.6	>300	>7.1	$7\ 10^4$
FeP_2	0 Li	0.084	0			
	4.6 Li; 0 V	39.2	23.7	13.5	2.7 ± 0.4	$7\ 10^4$
	2.75 Li; 0 V	81.4	49.2	18	2.8 ± 0.5	$7\ 10^4$
FeP_4	0 Li	0.15	0			
	6.0 Li; 0 V	12.6	0			
	6.8 Li; 0 V	40.4	12	110 ± 10	~5.0	$7\ 10^4$

[a] Metallic iron percentage deduced from the magnetization. Fe nanoparticles size deduced from fitting the ZFC/FC curves.

close to bulk α-Fe and particle radii exceeding 6 nm. For all other analyzed points of the electrochemical cycle the ZFC curves evidence a blocking temperature between 10 and 20 K corresponding to particle sizes around 3 nm.

FeP_2. Magnetic measurements were performed at the end of the first and second discharge (Figure 6) at 2 K and a ferromagnetic behavior was observed for both samples. We note that, in agreement with literature, the starting material FeP_2 is diamagnetic.[29] The value of the magnetization at the end of the first and second discharge is 40 and 81 Am^2/kg_{Fe}, respectively, corresponding to 18% and 36% of metallic iron, if we assume that the electrochemically formed iron carries a magnetic moment close to the bulk value. The first value is in quantitative agreement with the result obtained by Mössbauer spectroscopy (spectrum c in Figure 4), while the increase between first and second discharge is in qualitative agreement with the results obtained from spectrum h.

The particle size distribution was determined from fits of the ZFC-FC curves shown in Figure 6. The ZFC curve reveals a superparamagnetic behavior with a blocking temperature of about 12 K, contrary to the ferromagnetic behavior at room temperature of the FeP electrode at the end of the first discharge. The size of the Fe nanoparticles was calculated to 2.8 ± 0.4 nm. This value corresponds to the mean particle size found for FeP in the middle of the charge or discharge process.

At the end of the second discharge, the electrode also consists of superparamagnetic Fe nanoparticles with a blocking temperature of about 12 K. However, the FC curve cannot be fitted by a Curie−Weiss law. The interactions between particles are not negligible anymore and the size dispersion of the particles is too broad to be fitted accordingly. Nevertheless, one should notice that once again the sample is superparamagnetic contrary to FeP at the end of the second discharge.

FeP_4. Magnetic measurements were performed at the end of the first and second discharge (Figure 7) at 2 K and a hysteresis was observed for both samples. The value of the saturation magnetization at the end of the first and second discharge is 13 and 40 Am^2/kg_{Fe}, respectively.

As shown in Figure 7b, the electrode at the end of the first discharge does not display a superparamagnetic behavior. The ZFC curve does not present any maximum in the temperature range 2−260 K. The ZFC and FC curves display a hysteresis from 2 to 200 K, which is reminiscent of the hysteresis found in the M(H) curve. Such a behavior is typically found in spin glass systems, where paramagnetic species are in dipolar interactions leading to metastable states. According to XRD and Mössbauer spectroscopy, the phase formed during the discharge is a ternary compound Li_5FeP_4. This phase undoubtedly presents a high level of disorder as demonstrated by the broad XRD peaks and as it is usually the case for an electrochemically obtained phase. Therefore, there is a high probability that the iron sites are distributed statistically, resulting in a spin glass of paramagnetic Fe atoms. The ZFC/FC curve obtained on the electrode at the end of the second discharge displays almost the same shape except that the hysteresis is even more visible. In this case, and taking into account the magnetic moment of 40 A m^2 g^{-1} at 2 K, we assume that the susceptibility arises from both a spin glass contribution and from metallic iron formed electrochemically from the FeP and FeP_2 impurities in the starting material.

3.6. NMR Measurements. *FeP*. For the fully discharged FeP-2.3Li sample, no ^{31}P resonance could be observed, and a very broad ^7Li signal was recorded (Figure 8). The latter is close

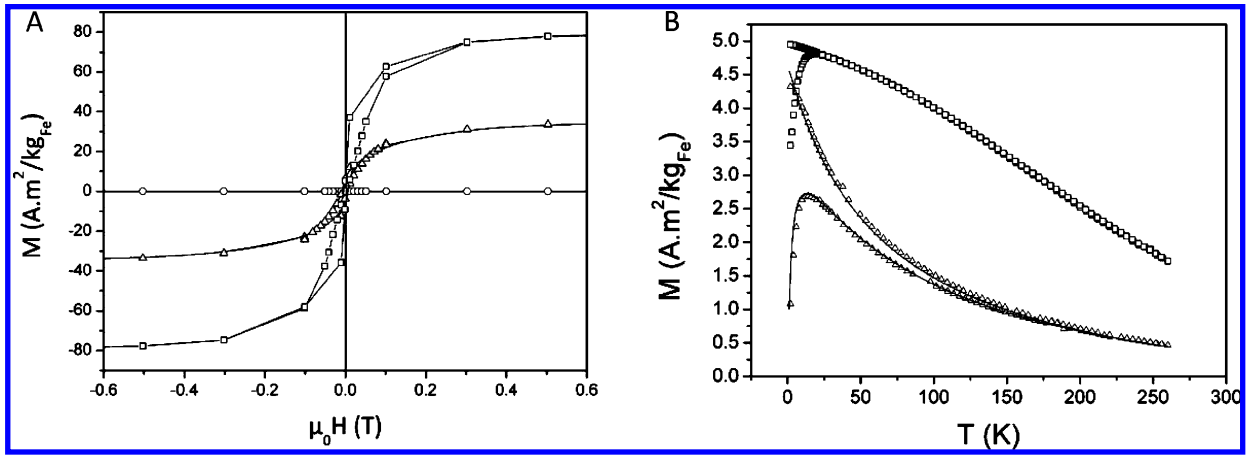

Figure 6. (A) Field dependence at 2 K of the magnetization of a FeP_2 electrode (starting material: open circles) at various depths of lithiation after first discharge (open triangles), and second discharge (open squares). (B) Magnetic susceptibilities of FeP_2 electrodes after first discharge (open circles) and calculated ZFC/FC (line).

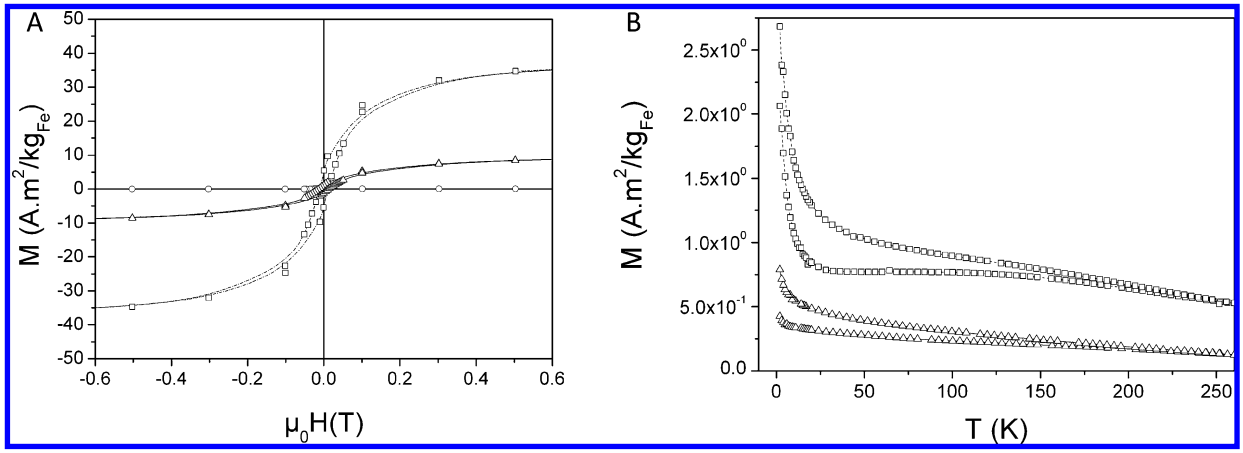

Figure 7. (A) Field dependence at 2 K of the magnetization of a FeP_4 electrode (starting material: open circles) at various depths of lithiation after first discharge (open triangles), and second discharge (open squares). (B) Magnetic susceptibilities of FeP_4 electrodes after first discharge (open triangles) and second discharge (open squares).

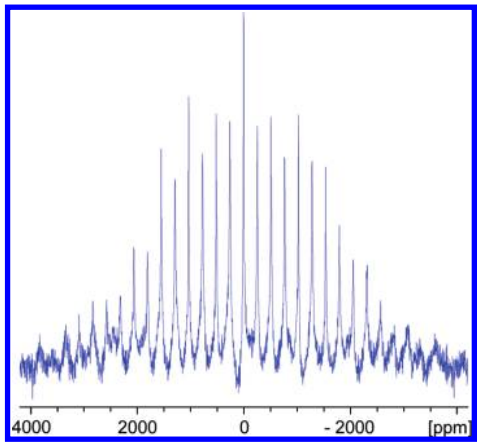

Figure 8. ^{7}Li MAS NMR spectrum for FeP-2.3Li (116 MHz, 30 kHz spinning).

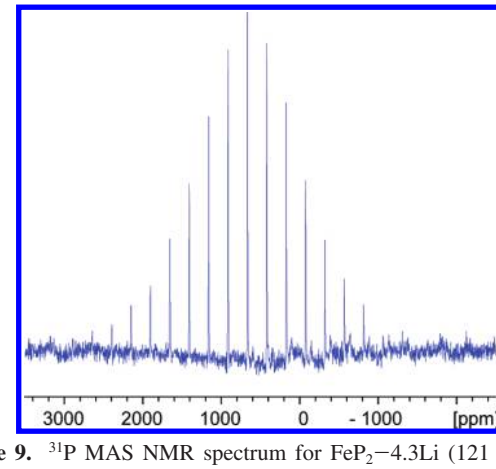

Figure 9. ^{31}P MAS NMR spectrum for FeP_2−4.3Li (121 MHz, 30 kHz spinning).

to 0 ppm, and therefore corresponds mostly to diamagnetic species present in the solid electrolyte interphase (SEI).

However, considering the width of the signal, one cannot exclude the presence of a signal at 2.9 ppm that would correspond to Li_3P.[30–32] The considerable width of the ^{7}Li signal and the nonobservability of the ^{31}P one suggest that the nuclei feel a very strong dipolar interaction with the paramagnetic Fe.

FeP_2. The ^{31}P MAS NMR spectrum for FeP_2−4.3Li (Figure 9) shows a signal corresponding to traces of remaining FeP_2 (in agreement with XRD and Mössbauer spectroscopy) but with a larger overall width (number of spinning sidebands) than for pure FeP_2.[30] This is clearly due again to dipolar interactions with electron spins from the paramagnetic iron in close proximity. Note that the intrinsic width of the ^{31}P MAS NMR signal of FeP[30] probably prevents its observation as traces in the presence of paramagnetic species. A very weak unidentified signal is also observable, with many broader spinning sidebands, that might originate from the ternary "Li_xFeP" compound. Like

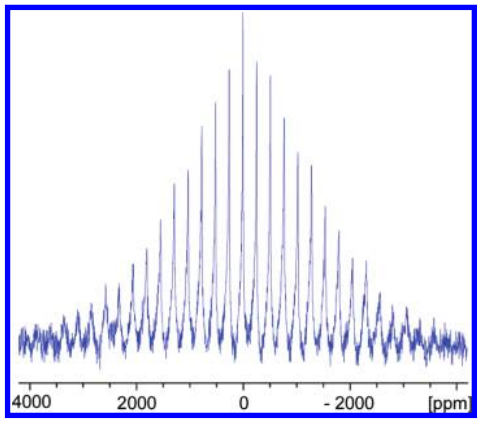

Figure 10. ^{7}Li MAS NMR spectrum of FeP_2-4.3Li (116 MHz, 30 kHz spinning).

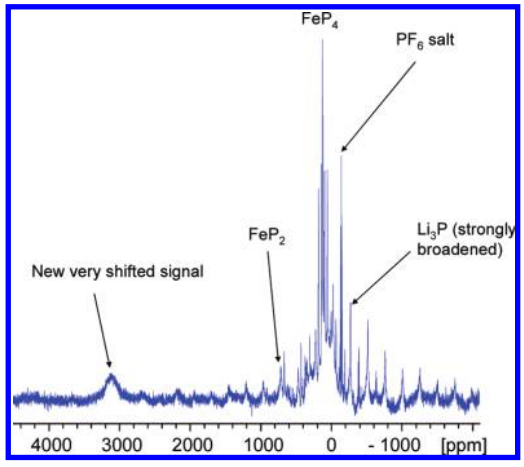

Figure 11. ^{31}P MAS NMR spectrum for FeP_4-5Li (121 MHz, 30 kHz spinning).

for FeP-2.3Li, Li_3P (−280 ppm) is not observed, probably due to its extreme proximity with paramagnetic iron.

The ^{7}Li MAS NMR spectrum for the same compound again shows a very broad signal (Figure 10), both in terms of number of spinning sidebands and of their width. This signal suggests the presence of a variety of Li species, each with a characteristic interaction strength with paramagnetic iron. Like for FeP-2.3Li, the resonance for Li_3P (if present) could be buried in this distribution of signals.

FeP_4. The ^{31}P MAS NMR spectrum of FeP_4-5Li (Figure 11) shows traces of PF_6 ions from the electrolyte, as well as signals from unreacted pristine FeP_4 and traces of FeP_2.[30] In addition, a very broad and shifted (3100 ppm) signal is observed that might correspond to a paramagnetic ternary Li_5FeP_4 compound. Finally, a weak signal corresponding to traces of Li_3P (−280 ppm) is also observed, with a large number of spinning sidebands, probably due to proximity with the paramagnetic ternary phase.

The ^{7}Li NMR spectrum of the same sample shows a signal close to 0 ppm, with less spinning sidebands than in the case of the lithiated FeP and FeP_2 compounds (in agreement with the absence of paramagnetic Fe and with the presence of a weaker magnetism due to the ternary Li_5FeP_4 compound). The broad and shifted ^{7}Li NMR response apparent at 35 ppm besides the 0 ppm one (Figure 12, zoom) corresponds most probably to the Li from this ternary phase. The ^{7}Li NMR response of traces of Li_3P (detected by ^{31}P NMR) might be hidden in the base of the 0 ppm signal.

4. Discussion

FeP, FeP_2. From the earlier study of FeP we deduced the simultaneous formation of Li_3P and metallic iron during the first discharge, according to the reaction mechanism $FeP + 3Li \rightarrow Li_3P + Fe$ as proposed in ref 10. Charging the cell to a potential of 1 V vs Li^+/Li (process A in Figure 2) corresponds to the reaction $Fe + Li_3P - xLi \rightarrow Li_{3-x}FeP$ with x close to 2. Further charging up to 2 V (process B) corresponds to the extraction of approximately one further lithium atom per FeP formula unit and causes the partial disappearance of Li_xFeP. As the Mössbauer parameters of this ternary phase and those of FeP remain rather constant over the whole charge/discharge process while only their relative proportions vary, we concluded that process B corresponds to a complete lithium extraction from a part of the ternary phase leading back to an FeP lattice with some Li_xFeP remaining, rather than a simple reduction of x in Li_xFeP at a constant Li_xFeP/FeP ratio. The second discharge to 0.5 V (process B′) leads to the transformation of some FeP to Li_xFeP and is the opposite of process B. Further discharge to 0 V (process A′) forms again Li_3P and metallic iron and is the opposite of process A.

For FeP_2, the first discharge leads to the simultaneous formation of Li_3P, metallic Fe, FeP, and Li_xFeP. The relative amount of metallic iron at the end of the first discharge is, however, much lower than for FeP (24% or 22% according to magnetic measurements or Mössbauer spectroscopy, respectively, as compared to 75% or 62% for FeP). From this combined analysis we can propose a partial conversion upon the first discharge of FeP_2 as defined by the following qualitative reaction schemes:

$$FeP_2 + yLi \rightarrow Fe + Li_3P + (FeP + Li_xFeP) + \varepsilon FeP_2 \quad (4)$$

The first plateau observed upon charge, at the same potential of 0.9 V as for FeP (A), causes an important part of the metallic iron to disappear and increases the Li_xFeP/FeP ratio. We therefore conclude that lithium is extracted from the Li_3P phase according to the same net reaction $Fe + Li_3P - xLi \rightarrow Li_{3-x}FeP$ as in FeP. The second plateau also occurs at the same potential as in FeP, i.e., at 1.1 V (B). It is characterized by a decrease of the relative amount of Li_xFeP and an increase of that of FeP. We thus attribute this plateau to a lithium extraction from the ternary phase with formation of FeP, in analogy to the mechanism proposed for FeP. At the end of charge the pristine FeP_2 is not restored.

$$\text{(A and B)} \qquad Fe + Li_3P + (FeP + Li_xFeP) + \varepsilon FeP_2 \rightarrow (FeP + Li_xFeP) + \varepsilon FeP_2 + yLi \quad (5)$$

The second discharge forms again metallic iron by reducing the amount of FeP. A transformation of FeP to metallic Fe and Li_3P with intermediate formation of Li_xFeP is thus proposed for the two-step discharge process in FeP_2, in analogy to FeP. The mechanism consuming residual FeP_2 during recharge and restoring it during the second discharge is, at present, unclear.

$$\text{(A' and B')} \qquad (FeP + Li_xFeP) + \varepsilon FeP_2 + yLi \rightarrow Fe + Li_3P + (FeP + Li_xFeP) + \varepsilon FeP_2 \quad (6)$$

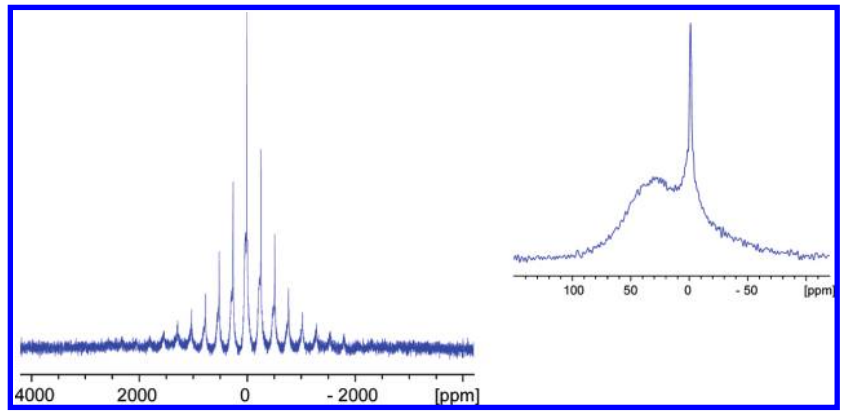

Figure 12. ^{7}Li MAS NMR spectrum of FeP_4-5Li (116 MHz, 30 kHz spinning).

Note that these eqs 4−6 cannot be quantitatively balanced based on the data available.

The proposed electrochemical mechanism for FeP_2 explains the large capacity loss during the first cycle (34%). The conversion process to form Li_3P and metallic Fe is only partially achieved on first discharge and - contrary to FeP - the starting material FeP_2 is not recovered on charge. The same intermediate Li_xFeP, FeP, Li_3P and Fe^0 phases than those previously observed for FeP are identified for FeP_2. For both FeP and FeP_2, the cycleability can be improved by limiting the potential window (see the Supporting Information, S1): 1850 and 1520 mAh/cm^3 volume capacities can be sustained, respectively, during several dozens of cycles when the $Fe + Li_3P - xLi \leftrightarrow Li_{3-x}FeP$ process at low potential is ruled out, which shows that the conversion reaction penalizes the cycleability.

Note that the electrochemical study reported in this article involves different mechanisms and not one unique and reversible process as previously reported in the literature.[33] The authors suggested an insertion mechanism instead of a conversion reaction on discharge, leading to the formation of a metastable and nanostructured $FexP-Li_yP-Fe_x$ electrode. This difference in the electrochemical behavior may arise from a spontaneous evolution of the electrode material toward a new equilibrium state once the discharge or charge process has been stopped and the external constraint of an imposed electrochemical potential is removed (open circuit condition).

We followed the evolution of an FeP electrode after its removal from the Swagelok cell at the end of its second discharge in order to check the stability of electrode materials. To this end several Mössbauer spectra were recorded over a period of four weeks after the end of the electrochemical test. The spectra are shown in Figure 13. It is worth noting that the material was enclosed in an airtight sample holder under argon atmosphere and that this sample holder remained in the cryostat under vacuum even for room temperature measurements, so that oxidation of the sample can be excluded. Spectrum 13a was recorded at 77 K immediately after the second discharge. It shows the sextet and singlet of magnetically blocked and superparamagnetic iron, respectively, and a sextet of magnetically ordered FeP, as described in.[11] Spectrum 13b was recorded at room temperature two days after the discharge was stopped. It still shows the presence of metallic iron, although the lines of the sextet collapse to an extremely broad singlet due to the higher fluctuation rate of the magnetization at room temperature as compared to 77 K. FeP gives rise to a doublet. Spectrum 13 c was recorded after five days. This and all following spectra were recorded on a reduced velocity scale providing better resolution in the range from −2 to +2 mm/s. After five days

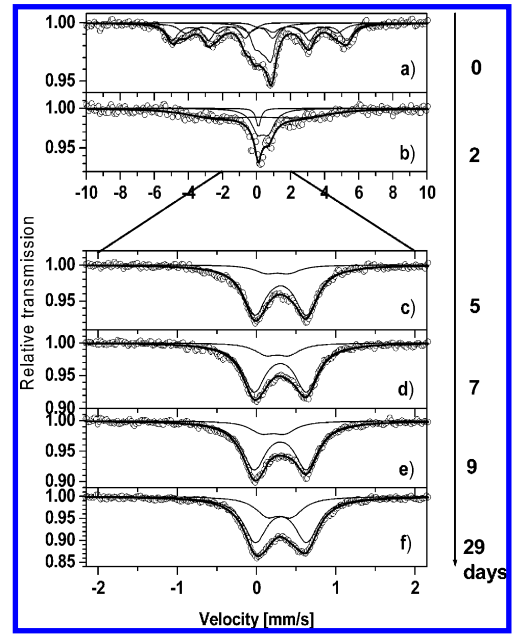

Figure 13. Evolution of a FeP electrode with time after two complete discharges. Mössbauer spectra recorded (a) immediately after the second discharge, and 2 (b), 5 (c), 7 (d), and 9 days (e) and 4 weeks (f) after the end of the electrochemical test. Spectrum (a) recorded at 77 K, and spectra (b−f) recorded at 295 K.

no metallic iron is found, neither magnetically blocked nor superparamagnetic. Instead, the doublet of the ternary phase Li_xFeP appears. Its intensity increases during the following three weeks (spectra 13 d to f). Spectrum 13 f can be considered as the new equilibrium state.

We followed the evolution of the open circuit voltage of identical cells after the first recharge and after two discharges over a period of two weeks. In the latter case the voltage rises from zero to 0.22 V (see Figure 14) which is the characteristic potential of process A′ seen in Figure 2 and which was associated in the preceding paragraph with the conversion of the ternary phase Li_xFeP to Li_3P and Fe^0. The open circuit voltage of a cell recharged to 2.5 V drops to 0.84 V which is the characteristic potential of the opposite process A, corresponding to the formation of the ternary phase from Li_3P and Fe^0. The hatched range in Figure 14 marks thus the potential window in which the ternary phase is stable. This tendency of the potential to evolve back to a value where Li_xFeP can be formed is not surprising as thermodynamical calculations have shown that LiFeP is more stable than mixtures of FeP, Li_3P, and Fe^0.[10]

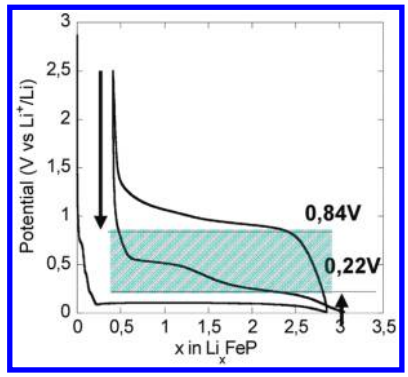

Figure 14. Open circuit voltages at equilibrium, attained 2 weeks after recharge and after second discharge, respectively.

Moreover, the reaction is facilitated by the fact that metallic iron is present in the form of highly reactive small particles of a few nanometers in diameter (see Table 3 for particle sizes derived from magnetic data) embedded in and in close contact with Li_3P, Li_xFeP, and residual FeP. The formation of a ternary phase from Li_3P and Fe^0 could thus proceed by atomic diffusion even at room temperature and consume the small iron particles within a few days. At the temperature of liquid nitrogen, however, the diffusion process is sufficiently showed down that the iron can be conserved as metallic particles over longer periods.

The same instability can be expected for FeP_2 electrodes as FeP_2 forms the same intermediate reaction products as FeP electrodes. Consequently, the mechanism reported in[33] can originate from the evolution of the FeP_2 electrode at 0 V.

FeP_4. The electrochemical mechanism governing charge and discharge of FeP_4 is obviously different from those observed for FeP and FeP_2. It is characterized by the direct formation of a ternary phase upon discharge and by lithium extraction from that ternary phase upon charge, allowing recovering the starting material. It is noteworthy that this lithium extraction occurs at a potential of 1.1 V, i.e. the same potential at which extraction from the ternary Li_xFeP occurs for FeP and FeP_2 (process B) while the formation of this ternary phase by lithiation occurs at 0.7 V, i.e. at the same potential where Li_xFeP is formed in the second discharge of FeP_2 and close to the 0.5 V where it is formed in FeP (process B'). The question arises whether this ternary phase is the same in all three cases. The ^{57}Fe Mössbauer parameters are identical within experimental error, indenpendently of the starting material, suggesting that the local environment of iron atoms is the same in all cases. However, we observe only for FeP_4 (i) a "Li_7MnP_4" fcc type phase by in situ XRD, (ii) a ^{31}P NMR signal characterizing a paramagnetic phase completely different from the signal observed for FeP and FeP_2, and (iii) a magnetic contribution from this phase.

FeP_4 cannot be classified in the conversion materials like FeP_x ($x = 1$ and 2) and numerous MP_x with M a middle transition metal.[34,35] The FeP_4/Li cell proceeds through classical insertion with the formation of an fcc Li_xFeP_4 phase. As shown above, the FeP_4 structure can be described as an infinite zig-zagging of chains of (FeP_6) octahedra sharing only edges. Three such octahedra constitute the linear units of the phase, as compared to four in 6-MnP_4. In a recent paper, we focused on the Li/Mn/P system, providing a comparative study of the electrochemical behaviors of the ternary Li_7MnP_4 and the binary MnP_4 materials.[36] Li_7MnP_4 has a cubic structure ($Fm3\bar{m}$) built on nearly isolated MnP_4 tetrahedra[20] while MnP_4 has a structure built on edge-shared MnP_6 octahedra.[37] We showed that the MnP_4 electrode undergoes a more or less reversible solid state (crystalline) transformation associated with the reaction $MnP_4 + 7Li \leftrightarrow Li_7MnP_4$ ($Fm3\bar{m}$).[8,36] We also reported that an additional process was clearly identified after the conversion process at low potential that decomposes Li_7MnP_4 into Li_3P + Mn°, responsible for the poor capacity retention of the electrodes. In charge, an amorphous weakly lithiated $Li_{\sim 1}MnP_4$ phase was formed, very similar to the charged Li_xVP_4 and Li_xTiP_4 electrodes.[38,39] By contrast to the MnP_4 (TiP_4, VP_4) electrochemical mechanism, no decomposition of Li_xFeP_4 into $Li_3P + Fe^0$ is achieved at 0 V. The small amount of Fe^0 detected by magnetic measurements is certainly due to the conversion of FeP and FeP_2 impuritites. Interestingly, this intermediate Li_xFeP_4 phase is easily obtained from an electrochemical route, whereas it has not yet been synthesized through classical ceramic routes. Work is in progress to find the high temperature synthesis conditions to prepare the crystallized Li_xFeP_4 phase, in order to deduce its crystallographic parameters and to compare its electrochemical behavior vs Li with that of FeP_4. Its occurrence in the electrode plays a key role in the cycleability of the FeP_4/Li cell as previously observed for the Li_xMP_4 electrodes. From a crystallographic point of view, the FeP_6 octahedra of the FeP_4 structure share some of their edges and/or corners and the P atoms form a 3D network of relative covalent P−P bonds within each double layer (see Figure 1). In NMR spectra, unusually strong J couplings were observed, fully consistent with the existence of very covalent P−P bonds.[30] As previously shown for the Mn phase, it can be foreseen that the $MP_4 \leftrightarrow Li_7MP_4$ transformation (M: transition metal) occurs by cleavage of the P−P bonds at the time of Li insertion, resulting in cubic close packed phosphorus layers in Li_xMP_4. On charge, however, the reverse process does not regenerate a crystalline FeP_4 structure as observed for Mn-phosphide, since no Bragg peak appears in the X-ray diffraction pattern collected at 2 V (not shown here). Instead, an X-ray amorphous "FeP_4" phase is formed.

5. Concluding Remarks

The study of the reactivity of Li versus FeP_x phases with $x = 0.33$, 0.5, 1, 2, and 4 has clearly demonstrated the impact of the Fe/P ratio and/or the structural or electronic properties on the electrode performance. The phosphorus richer phases present a high reactivity vs Li, while iron richer phases ($x = 0.33$, 0.5) did not show any reactivity.[19] This demonstrates that a P-redox mechanism occurs in the cycling of batteries based on iron phosphides.

Electronic structure calculations describe a more localized behavior and a less metallic redox entity when x increases in FeP_x.[40] These electronic properties can explain an insertion type electrochemical behavior for FeP_4 in contrast to the conversion type process for FeP or FeP_2.

The numerous transition metal phosphides reported so far display different redox reactions depending on the 3d-transition metal. With early transition metals (M = Ti and V), lithium reaction proceeds through insertion type mechanisms, while with late transition metals (M = Co and Ni), it generally proceeds through the conversion of MP_y into a composite electrode made of metallic nanosized particles embedded in a Li_3P matrix described by the reaction $MP_y + 3yLi \rightarrow yLi_3P + M°$. This work demonstrated that with central transition metals M = Mn and Fe both types of processes may occur and that they represent a boundary in the first 3d transition metal line.

Furthermore the eqs 4−6 given above cannot be quantitatively balanced. In addition, as discussed in the case of FeP_2 and FeP, thermodynamic equilibrium is difficult to reach, and kinetic limitations partially govern the actual global reaction. Besides

the present work has demonstrated the instability of the composite electrode Li_3P/Fe^0 formed at the end of the discharge of FeP and FeP_2. Once the external constraint of an electrochemical potential of 0 V versus Li^+/Li^0 is lifted (open circuit condition), a reaction channel is open toward a thermodynamically more stable phase (Li_xFeP). This fact is of importance in several domains: (i) in basic research on electrode materials where all analyses of the material by ex-situ techniques should be carried out immediately after the end of the electrochemical test run; (ii) in technical applications as a battery electrode where it is a frequent situation that the battery remains for a longer time in a partly or completely discharged state before being recharged. Here it has to be checked whether the new equilibrium state allows to resume cycling with the same performances as a newly made battery or whether measures can be taken (e.g., by means of appropriate electronics) in order to avoid the relaxation of the battery when not in use.

Acknowledgment. Authors thank M. L. Doublet for helpful discussions which often enabled a predictive vision of the mechanism of FeP_x electrodes. This research was performed in the framework of the ALISTORE Network of Excellence (Contract No. SES6 - CT-2003-503532) funded by the European Union. We thank the ADEME (Agence de l'Environnement et de la Maîtrise de l'Energie, France) for its financial support through the Ph.D. grants of S.B.

Supporting Information Available: Figure showing capacity retention of the FeP_x/Li cells ($x = 1$, 2, and 4) on various potential windows. This material is available free of charge via the Internet at http://pubs.acs.org.

References and Notes

(1) Dahn, J. R.; Zheng, T.; Liu, Y.; Xue, J. S. *Science* **1995**, *270*, 590.
(2) Alcantara, R.; Jimenez-Mateos, J. M.; Tirado, J. L. *J. Electrochem. Soc.* **2002**, *149*, 201.
(3) Inaba, M.; Yoshida, H.; Ogumi, Z. *J. Electrochem. Soc.* **1996**, *143*, 2572.
(4) Nagaura, T.; Tozawa, K. *Prog. Batt. Solar Cells* **1990**, *9*, 209.
(5) Bichat, M. P.; Politova, T.; Pfeiffer, H.; Tancret, F.; Monconduit, L.; Pascal, J. L.; Brousse, T.; Favier, F. *J. Power Sources* **2004**, *136*, 80–87.
(6) Park, C.-M.; Sohn, H.-J. *Adv. Mater.* **2007**, *19* (18), 2465–2468.
(7) Gillot, F.; Boyanov, S.; Dupont, L.; Doublet, M.-L.; Morcrette, M.; Monconduit, L.; Tarascon, J.-M. *Chem. Mater.* **2005**, *17* (25), 6327–6337.
(8) Souza, D. C. S.; Pratong, V.; Jacobson, A. J.; Nazar, L. F. *Science* **2002**, *296*, 2012–2015.
(9) Boyanov, S.; Gillot, F.; Monconduit, L. *Ionics* **2008**, *14*, 125–130.
(10) Boyanov, S.; Bernardi, J.; Gillot, F.; Dupont, L.; Womes, M.; Tarascon, J.-M.; Monconduit, L.; Doublet, M.-L. *Chem. Mater.* **2006**, *18*, 3531–3538.
(11) Boyanov, S.; Womes, M.; Monconduit, L.; Zitoun, D. *Chem. Mater.* **2009**, *21*, 3684−3692.
(12) Juza, R.; Langer, R. *Z. Anorg. Allg. Chem.* **1968**, *361*, 58.
(13) Morcrette, M.; Gillot, F.; Monconduit, L.; Tarascon, J. M. *Electrochem. Solid-State Lett.* **2003**, *6*, 4.
(14) Kündig, W. *Nucl. Instr. Methods* **1969**, *75*, 336.
(15) Aydinol, M. K.; Kohan, A. F.; Ceder, G.; Cho, K.; Joannopoulos, J. *Phys. Rev. B* **1997**, *56*, 1354.
(16) Rundqvist, S. *Acta Chem. Scand.* **1962**, *16*, 287.
(17) Dahl, E. *Acta Chem. Scand.* **1969**, *23*, 2677.
(18) Jeitschko, W.; Braun, D. J. *Acta Crystallogr. B* **1978**, *34*, 3196.
(19) Boyanov, S. Ph.D. Thesis, University of Montpellier: Montpellier, France, 2008.
(20) Juza, R.; Bohmann, T. *Z. Anorg. Allg. Chem.* **1961**, *308*, 159.
(21) Langer, K.; Juza, R. *Z. Anorg. Allg. Chem.* **1968**, *361*, 74.
(22) Juza, R.; Langer, K.; von Benda, K. *Angew. Chem., Int. Ed.* **1968**, *7*, 5.
(23) Monconduit, L.; Tillard, M.; Belin, C. *J. Solid State Chem.* **2001**, *156*, 37.
(24) Wäppling, R.; Häggström, L.; Rundqvist, S.; Karlsson, E. *J. Solid State Chem.* **1971**, *3*, 276–292.
(25) Van der Woude, F.; Dekker, A. J. *Phys. Status Solidi* **1965**, *9*, 775.
(26) Hendriksen, P. V.; Linderoth, S.; Lindgard, P. A. *Phys. Rev. B* **1993**, *48*, 7259–7273.
(27) Bødker, F.; Mørup, S.; Linderoth, S. *J. Magn. Magn. Mater* **1995**, *140−144*, 373–374.
(28) Grandjean, F.; Gérard, A.; Krieger, U.; Heiden, C.; Braun, D. J.; Jeitschko, W. *Solid State Commun.* **1980**, *33*, 261.
(29) Hulliger, F.; Mooser, E. *J. Phys. Chem. Solids* **1965**, *26*, 429.
(30) Bekaert, E.; Bernardi, J.; Boyanov, S.; Monconduit, L.; Doublet, M. L.; Menetrier, M. *J. Phys. Chem. C* **2008**, *112* (51), 20481–20490.
(31) Leon, B.; Correor, J. I.; Tirado, J. L.; Perez-Vicente, C. *J. Electrochem. Soc.* **2006**, *153* (10), A1829.
(32) Gillot, F.; Ménétrier, M.; Bekaert, E.; Dupont, L.; Morcrette, M.; Monconduit, L.; Tarascon, J. M. *J. Power Sources* **2007**, *172* (2), 877–885.
(33) Silva, D. C. C.; Crosnier, O.; Ouvrard, G.; Greedan, J.; Safa-Sefat, A.; Nazar, L. F. *Electrochem. Solid-State Lett.* **2003**, *6*, A162.
(34) Alcantara, R.; Tirado, J. L.; Jumas, J. C.; Monconduit, L.; Olivier-Fourcade, J. *J. Power Sources* **2002**, *109*, 308.
(35) Pralong, V.; Souza, D. C. S.; Leunge, K. T.; Nazar, L. F. *Electrochem. Commun.* **2002**, *4*, 516.
(36) Gillot, F.; Monconduit, L.; Doublet, M.-L. *Chem. Mater.* **2005**, *17* (23), 5817–5823.
(37) Jeitschko, W.; Donohue, P. C. *Acta Crystallogr., Sec. B* **1975**, *31*, 574.
(38) Doublet, M.-L.; Lemoigno, F.; Gillot, F.; Monconduit, L. *Chem. Mater.* **2002**, *14*, 4126.
(39) Bichat, M.-P.; Gillot, F.; Monconduit, L.; Favier, F.; Morcrette, M.; Lemoigno, F.; Doublet, M.-L. *Chem. Mater.* **2004**, *16*, 1002.
(40) Bernardi, J. Ph.D. Thesis, University of Montpellier: Montpellier, France, 2008.

JP906080J